

Modelling of oscillations in two-dimensional echo-spectra of the Fenna–Matthews–Olson complex

This article has been downloaded from IOPscience. Please scroll down to see the full text article.

2012 New J. Phys. 14 023018

(<http://iopscience.iop.org/1367-2630/14/2/023018>)

View [the table of contents for this issue](#), or go to the [journal homepage](#) for more

Download details:

IP Address: 132.199.144.50

The article was downloaded on 08/02/2012 at 12:31

Please note that [terms and conditions apply](#).

Modelling of oscillations in two-dimensional echo-spectra of the Fenna–Matthews–Olson complex

Birgit Hein^{1,4}, Christoph Kreisbeck¹, Tobias Kramer^{1,2,4} and Mirta Rodríguez³

¹ Institut für Theoretische Physik, Universität Regensburg, 93040 Regensburg, Germany

² Department of Physics, Harvard University, Cambridge, MA 02138, USA

³ Instituto de Estructura de la Materia CSIC, C/ Serrano 121, 28006 Madrid, Spain

E-mail: birgit.hein@physik.uni-regensburg.de and tobias.kramer@mytum.de

New Journal of Physics **14** (2012) 023018 (20pp)

Received 7 October 2011

Published 7 February 2012

Online at <http://www.njp.org/>

doi:10.1088/1367-2630/14/2/023018

Abstract. Recent experimental observations of time-dependent beatings in the two-dimensional echo-spectra of light-harvesting complexes at ambient temperatures have opened up the question of whether coherence and wave-like behaviour play a significant role in photosynthesis. We carry out a numerical study of the absorption and echo-spectra of the Fenna–Matthews–Olson (FMO) complex in *Chlorobium tepidum* and analyse the requirements in the theoretical model needed to reproduce beatings in the calculated spectra. The energy transfer in the FMO pigment–protein complex is theoretically described by an exciton Hamiltonian coupled to a phonon bath which accounts for the pigments' electronic and vibrational excitations, respectively. We use the hierarchical equations of motions method to treat the strong couplings in a non-perturbative way. We show that the oscillations in the two-dimensional echo-spectra persist in the presence of thermal noise and static disorder.

⁴ Authors to whom any correspondence should be addressed.

Contents

1. Introduction	2
2. Exciton model of the Fenna–Matthews–Olson (FMO) complex	3
3. Absorption spectra of the FMO complex	6
3.1. Absorption spectra obtained by different propagation methods	8
3.2. Broadening of the spectral lines	9
4. Two-dimensional (2D) echo-spectroscopy	10
4.1. Numerical results for the 2D echo-spectrum of the FMO complex	12
5. Conclusions	16
Acknowledgments	17
References	17

1. Introduction

Light-harvesting complexes are that part of photosynthetic systems that channel energy from the antenna to the reaction centre. One of the most studied complexes is the Fenna–Matthews–Olson (FMO) complex [1–3], which is part of the photosynthetic apparatus of green sulfur bacteria. The observation of long-lasting beatings, up to 1.8 ps at $T = 77$ K in time-resolved two-dimensional (2D) spectra [4–6], has generated much interest in the theoretical modelling of the process of energy transfer through light-harvesting complexes. Recently, molecular-dynamics simulations started developing a more microscopic picture of the dynamics [7, 8], but an atomistic and fully quantum-mechanical model of the whole process reproducing the experimentally obtained spectra is not available. Therefore, theoretical models treat the light-harvesting pigment–protein complex as an exciton system coupled to a bath which accounts for the vibrational modes of the pigments.

The choreography of the exciton-energy transfer can be elucidated with 2D echo-spectroscopy using three laser pulses which hit the sample within several femtoseconds time spacings. The experimentally measured 2D echo-spectra of the complex show a variety of beating patterns with oscillation periods roughly consistent with the differences in eigenenergies of the excited system obtained from fits to the absorption and 2D echo-spectra [5]. At long delay times between pump and probe pulses the system displays relaxation to the energetically lowest-lying exciton eigenstates as expected from interactions between the electronic degrees of freedom and the vibrational modes of the complex which drive the system into a state of thermal equilibrium [9].

One main goal of the research in this field is to clarify the role of a disordered and fluctuating environment in the energy-transfer efficiency. Theoretical quantum-transport studies show that the energy transfer in these systems results from a balance between coherent and dissipative dynamics [10, 11]. Calculations at room temperature also show that the optimal energy-transport efficiencies appear as a compromise between coherent dynamics and thermal fluctuations [12].

Another open question in the theoretical study of these systems is the description of experimental observables, i.e. the absorption and the 2D echo-spectra. Most of the theoretical studies analyse the beatings in the population dynamics and compare them with those observed in the experimentally measured 2D echo-spectra. However, the 2D echo-spectrum reflects

different information from the population dynamics and needs to be calculated and analysed separately in detail. In principle, techniques such as quantum state and process tomography made out of a sequence of 2D echo-spectra can be used to map out the complete density matrix [13]. In contrast to energy-transfer efficiency studies where an initial excitation enters the complex at specific sites close to the antenna, in 2D echo-spectra the whole complex is simultaneously excited. Also the two-exciton manifold yields prominent contributions to the signal, resulting in negative regions in the 2D echo-spectra.

The non-perturbative calculation of 2D echo-spectra presents a considerable computational challenge owing to the presence of two excitons giving rise to excited state absorption and the requirement to consider ensemble averages over differently orientated complexes with slightly varying energy levels. Previous calculations have used Markovian approximations [14, 15] or exclude the double-exciton manifold [16]. In addition, the systematic study of beatings in a series of 2D echo-spectra requires an effective means of calculating a huge number of such spectra. So far, no theoretical method has been able to describe the long-lasting beatings in the time-resolved 2D spectra [14, 16, 17]. One possible explanation for the persistence of long coherence times has been the sluggish absorption of the reorganization energy by the molecule, which requires theoretical descriptions that go beyond the Markovian approximation and the rotating wave approximation [18]. The hierarchical equations of motions (HEOM), first developed by Tanimura and Kubo [19] and subsequently refined in [20–23], show oscillations in the dynamics of the exciton populations that persist even at temperature $T = 300$ K [24, 25]. The HEOM include the reorganization process in a transparent way and are directly applicable to computations at physiological temperatures. A calculation at temperature 77 K of the 2D echo-spectra with the HEOM method has recently been performed by Chen *et al* [17], which does not display the strong beatings observed experimentally. Chen *et al* conclude that the agreement between theory and experiments needs to be improved. Here, we analyse the conditions under which the theoretical calculations give better agreement with the experimental results. We calculate the absorption and 2D echo-spectra in a temperature range between 77 and 277 K using the HEOM and investigate the role of pigment and protein vibrations in the calculated spectra. We systematically discuss the parameters needed to obtain results that agree better with the experimentally measured spectra. We discuss the role of static disorder in the shapes of the peaks and the appearance of beatings in the time-resolved 2D echo-spectrum and their robustness against temperature changes and static disorder.

This paper is organized as follows: the exciton model and the HEOM are introduced in section 2. The absorption spectra and the line shapes obtained from the HEOM model of the FMO complex are analysed in section 3, where we compare different methods of performing rotational averages. In section 4 we discuss the 2D spectrum and analyse how disorder affects it. Furthermore, we analyse the persistence of beatings in the spectra as a function of delay time for several temperatures and with and without static disorder.

2. Exciton model of the Fenna–Matthews–Olson (FMO) complex

The FMO complex described by Fenna, Matthews and Olson [2, 3] is a pigment–protein complex that channels the energy in the photosynthetic apparatus in green sulfur bacteria. The FMO complex is arranged as a trimer with the different subunits interacting weakly with each other. We therefore restrict our study to a single subunit which contains eight bacteriochlorophyll molecules (BChls) [26, 27]. The BChl pigments, which are wrapped in

a protein environment, can be electronically excited and are coupled due to dipole–dipole interactions. The BChls form a network that guides energy from the antenna to the reaction centre. Since the eighth BChl is only loosely bound, it usually detaches from the others when the system is isolated from its environment to perform experiments [26, 28]. Therefore, we do not take the eighth into account and we describe the energy transfer using the seven-site Frenkel exciton model [29–31]. The single-exciton manifold is given by

$$H_e^{1\text{ex}} = \sum_{k=1}^{N_{\text{sites}}} \epsilon_k |k\rangle\langle k| + \sum_{k>l} J_{kl} (|k\rangle\langle l| + |l\rangle\langle k|) \quad (1)$$

with $N_{\text{sites}} = 7$. The state $|k\rangle$ corresponds to an electronic excitation of BChl $_k$ with site energy ϵ_k . Dipole–dipole couplings between different chromophores yield the inter-site couplings J_{kl} , which lead to a delocalization of the exciton over all BChls. The site energies of the BChls $\epsilon_k = \epsilon_k^0 + \lambda_k$ consist of ‘zero-phonon energies’ ϵ_k^0 , and a term due to the reorganization Hamiltonian $H_{\text{reorg}} = \sum_{k=1}^{N_{\text{sites}}} \lambda_k |k\rangle\langle k|$. The reorganization energy $\lambda_k = (\sum_i \hbar \omega_i q_i^2 / 2)_k$ denotes the energy that is removed from the system in order to adjust the vibrational coordinates to the new equilibrium value [24, 31, 32]. Here, q_i denotes a dimensionless displacement of the i th oscillator measured in units of $\sqrt{\hbar / (m_i \omega_i)}$, where m_i and ω_i are the mass and frequency of the i th oscillator. The vibrational modes of the BChl are modelled as a set of harmonic oscillators $H_{\text{phon}} = \sum_i \hbar \omega_i b_i^\dagger b_i$. The vibrational environment couples linearly to the exciton system $H_{\text{ex-phon}} = \sum_{k=1}^{N_{\text{sites}}} (\sum_i \hbar \omega_i q_i (b_i + b_i^\dagger))_k |k\rangle\langle k|$ and induces fluctuations in the site energies. We neglect correlations between the vibrations at different sites and model the coupling strength by a structureless spectral density

$$J(\omega) = 2\lambda \frac{\omega\gamma}{\omega^2 + \gamma^2}, \quad (2)$$

where we assume identical couplings $\lambda_k = \lambda$ at each site. This choice of spectral density facilitates the use of the HEOM method since the time-dependent bath correlations then assume an exponential form. For the FMO complex a variety of spectral densities is discussed in the literature, where some are a parametrization of experimental fluorescence spectra [33], while others are extracted from molecular dynamics simulations [34]. We use the model Hamiltonian for *Chlorobium tepidum* given in [14]. The Hamiltonian originates from previous calculations in [35, 36]. Cho *et al* [14] changed the coupling constant between BChl 5 and BChl 6 and obtained new site energies from a fit to experimental results. While the period of oscillations in 2D echo-spectra depends on the resulting eigenenergies, we find that the appearance of oscillations is not affected. The Hamiltonian of [14] has been used in previous studies of 2D echo-spectra [14, 16, 17] and facilitates comparisons between the different approaches. In the site basis $\{|k\rangle\}$ the matrix elements read

$$H_e^{1\text{ex}} = \begin{pmatrix} 280 & -106 & 8 & -5 & 6 & -8 & -4 \\ -106 & 420 & 28 & 6 & 2 & 13 & 1 \\ 8 & 28 & 0 & -62 & -1 & -9 & 17 \\ -5 & 6 & -62 & 175 & -70 & -19 & -57 \\ 6 & 2 & -1 & -70 & 320 & 40 & -2 \\ -8 & 13 & -9 & -19 & 40 & 360 & 32 \\ -4 & 1 & 17 & -57 & -2 & 32 & 260 \end{pmatrix} + \lambda_S \mathbf{1} \quad (3)$$

in units of cm^{-1} , where we have added an energy shift $\lambda_S = 12\,075\text{ cm}^{-1}$ to the diagonal elements of the exciton Hamiltonian H_e^{lex} to shift the positions of the eigenenergies to the frequency range of the figures in [14]. We set the parameters of the spectral density to $\lambda = 35\text{ cm}^{-1}$ and $\gamma^{-1} = 50\text{ fs}$. These parameters are chosen to provide the best agreement to the smooth part of the spectral density in [33], where the low-frequency component of the spectral density was fitted to fluorescence line narrowing spectra [37]. Since a single Lorentz–Drude peak is not sufficient to accurately reproduce the smooth part of the spectral density of [33], we choose the parameters to obtain agreement within a factor of 1.2–1.5 in the energy range of 100–150 cm^{-1} , which corresponds to the typical difference between the exciton energies.

The HEOM approach rewrites time non-local effects into a hierarchy of coupled equations of motion for a set of auxiliary matrices $\sigma^{\vec{n}}$. The superscript \vec{n} is a vector of N_{sites} entries, where n_k gives the order to which the bath of BChl_k is taken into account. The reduced density matrix $\rho(t) = \text{tr}_{\text{phonon}} R(t)$ describing the exciton system is obtained after tracing out the vibrational degrees of freedom. The time evolution of the reduced density matrix is given by

$$\frac{d}{dt}\rho(t) = -i\mathcal{L}_e\rho(t) + \sum_{k=1}^{N_{\text{sites}}} \Phi_k \sigma^{\vec{e}_k}(t) \quad (4)$$

with

$$\frac{d}{dt}\sigma^{\vec{n}}(t) = -\left(i\mathcal{L}_e + \sum_{k=1}^{N_{\text{sites}}} \gamma n_k\right) \sigma^{\vec{n}}(t) + \sum_{k=1}^{N_{\text{sites}}} \Phi_k \sigma^{\vec{n}+\vec{e}_k}(t) + \sum_{k=1}^{N_{\text{sites}}} n_k \Theta_k \sigma^{\vec{n}-\vec{e}_k}(t). \quad (5)$$

\mathcal{L}_e is the Liouville operator of the coherent exciton dynamics and we define \vec{e}_k as the k th unit vector with $N_{\text{sites}} = 7$ entries. The operators Φ_k and Θ_k are defined by their action on a test operator A :

$$\Phi_k A = iV_k^\times A, \quad (6)$$

$$\Theta_k A = i\left(\frac{2\lambda_k}{\beta\hbar^2} V_k^\times A - i\frac{\lambda_k\gamma}{\hbar} (|k\rangle\langle k|A + A|k\rangle\langle k|)\right), \quad (7)$$

where $V_k^\times A = [|k\rangle\langle k|, A]$. The auxiliary matrices are initialized to $\sigma^{\vec{n}}(0) = 0$ for $\vec{n} \neq \vec{0}$ and $\sigma^{\vec{0}}(0) = \rho(t)$ [24]. The hierarchy is truncated for sufficiently large $N_{\text{max}} = \sum_{k=1}^{N_{\text{sites}}} n_k$, where the diagonal coupling in (5) becomes dominant. For the parameters used in the calculation, reorganization energy $\lambda = 35\text{ cm}^{-1}$ and phonon relaxation time scale $\gamma^{-1} = 50\text{ fs}$, we verified that the relative differences in the interesting energy region of the absorption spectrum using $N_{\text{max}} = 4$ versus $N_{\text{max}} = 12$ are below 0.13%. In the 2D echo-spectrum we compared the rephasing stimulated emission diagram for $N_{\text{max}} = 4$ and 12 and found a difference of less than 0.07% of the amplitude. We therefore consider a truncation at $N_{\text{max}} = 4$ sufficient for reaching converged results. The derivation of the hierarchy stated in (4) and (5) relies on a high-temperature approximation. For a temperature of 77 K the high-temperature approximation is not valid and low-temperature correction terms have to be included [25]. Within the low-temperature correction we replace

$$\begin{aligned} \mathcal{L}_e &\rightarrow \mathcal{L}_e - \sum_{k=1}^{N_{\text{sites}}} \frac{2\lambda_k}{\beta\hbar^2} \frac{2\gamma}{v_1^2 - \gamma^2} V_k^\times V_k^\times, \\ \Theta_k &\rightarrow \Theta_k - \frac{2\lambda_k}{\beta\hbar^2} \frac{2\gamma^2}{v_1^2 - \gamma^2} V_k^\times, \end{aligned} \quad (8)$$

where $\nu_1 = 2\pi/\beta\hbar$ is the first bosonic Matsubara frequency following [25]. Agreement with [38] and proper thermalization to the Boltzmann distribution [12] confirm that the first-order correction in (8) is indeed sufficient. A further improvement in the low-temperature correction can be attained by including higher Matsubara terms. Recently, also a Padé spectrum decomposition was proposed [39, 40] that shows a faster convergence than the Matsubara decomposition.

The numerical evaluation of the HEOM requires us to propagate a large number of auxiliary matrices. Although the number of auxiliary matrices can be reduced by a scaled HEOM approach [41, 42] as well as by advanced filtering techniques [41], the HEOM are computationally very demanding, which sets limits to treatable system sizes. For 2D echo-spectroscopy one has to propagate the set of auxiliary matrices not only for a huge number of time steps (typically of the order of 10^5), but also the dimension of the auxiliary matrices gets enlarged since excited state absorption requires us to extend the exciton Hamiltonian to the two-exciton manifold. We overcome the computational limitation by using a GPU (Graphics Processing Unit) implementation where the computation time goes down with the number of cores on a single GPU [12]. For example, on a single NVIDIA C2050 graphics board we obtain a 450-fold speedup compared to an equivalent single-core CPU implementation. With our efficient GPU algorithm the computation time for a 2D spectrum is reduced to 50 min on a single GPU.

3. Absorption spectra of the FMO complex

Spectroscopy provides a tool that gives direct insight into the energy states of a quantum system. Absorption spectroscopy is used to identify the energy eigenstates and their interaction strengths with the radiation field, expressed in terms of dipole moments. The energy eigenstates and the dipole moments are commonly identified with the peak position and the peak areas, respectively. The spectral peaks are broadened due to the interaction of the energy eigenstates with the remaining degrees of freedom of the system. For an ensemble of light-harvesting complexes, the coupling of the electronic dynamics to the vibrational modes and the presence of fluctuations in the energy levels, due to e.g. the motion of surrounding proteins, broaden the absorption peaks.

To calculate absorption spectra, we have to expand the system and add the ground state $|0\rangle$ to our basis. The Hamiltonian is thus extended to an 8×8 block matrix

$$H_e^{1D} = \begin{pmatrix} H_e^{\text{gs}} & 0 \\ 0 & H_e^{\text{lex}} \end{pmatrix}, \quad (9)$$

where we have chosen the zero exciton energy $H_e^{\text{gs}} = 0$ and H_e^{lex} is the 7×7 matrix defined in (3).

Using the same block structure as in (9), the dipole matrix that governs the photon–exciton conversion is constructed as

$$\mu = \begin{pmatrix} 0 & \mu_{1\text{ex}}^- \\ \mu_{1\text{ex}}^+ & 0 \end{pmatrix}, \quad (10)$$

where $\mu_{1\text{ex}}^+ = \mu_{1\text{ex}}^{-\text{T}}$ and the zero to single excitation dipole block

$$\mu_{1\text{ex}}^+ = \sum_{k=1}^{N_{\text{sites}}} \mu_k |k\rangle \langle 0| \quad (11)$$

is defined using the seven dipole moments μ_k that give the excitation of BChl_k by the laser pulse.

The absorption spectrum is calculated as

$$I_{1D}(\omega) = \left\langle \int_0^\infty dt e^{i\omega t} \text{tr} (\mu(t)\mu(0)\rho_0) \right\rangle_{\text{rot}}, \quad (12)$$

where $\rho_0 = |0\rangle\langle 0|$ is the density operator for no excitation and we assume δ -shaped laser pulses. The different methods for performing the rotational average denoted by $\langle \cdot \rangle_{\text{rot}}$ are detailed below. The time evolution of the dipole operators in (12) is given by $\mu(t) = e^{iH_c^{\text{1D}}(t)/\hbar} \mu e^{-iH_c^{\text{1D}}t/\hbar}$.

In the FMO complex the seven BChl molecules have a fixed orientation with respect to each other. Within this configuration each BChl has a dipole vector \vec{d}_k that characterizes its interaction with light. We consider the dipole vectors of the BChls to be along the connection line of two nitrogen atoms N_B-N_D [43], whose positions we obtain from the protein data bank [26, 44]. The norm of \vec{d}_k accounts for the strength of the dipole and we assume that $|\vec{d}_k| = d$ since all BChl molecules are identical. For the simulations we choose $d = 1$. Given a polarization direction of the laser $\vec{l} = (\sin \beta \cos \gamma, \sin \beta \sin \gamma, \cos \beta)$, where $\gamma \in [0, 2\pi)$ and $\beta \in [0, \pi]$, the dipole moments in (11) read

$$\mu_k = \vec{d}_k \cdot \vec{l}. \quad (13)$$

Typical experiments are performed using the spectroscopy of a sample solution and many FMO complexes are illuminated at the same time. Each of them is randomly orientated with respect to the electric field in the laser pulse. If we assume that a coherent dynamics expression (12) is readily evaluated in eigenbasis as

$$\langle \text{tr}(\mu(t)\mu(0)\rho_0) \rangle_{\text{rot}} = \frac{1}{4\pi} \sum_{j=1}^7 e^{-iE_j t/\hbar} \int_0^{2\pi} d\gamma \int_0^\pi d\beta \sin \beta \left(\sum_{k=1}^7 \vec{d}_k \cdot \vec{l} v_k^j \right)^2 \quad (14)$$

$$= \sum_{j=1}^7 \bar{\mu}_{E_j}^2 e^{-iE_j t/\hbar}, \quad (15)$$

where E_j is the j th eigenenergy and $v_k^j = \langle E_j | k \rangle$ denotes the overlap of the k th state in site basis with the j th eigenstate. The integrationally averaged dipole moments in eigenbasis are

$$\bar{\mu}_{E_j}^2 = \frac{1}{4\pi} \int_0^{2\pi} d\gamma \int_0^\pi d\beta \sin \beta \left(\sum_{k=1}^7 \vec{d}_k \cdot \vec{l} v_k^j \right)^2 = \frac{1}{3} \sum_{k,m=1}^7 v_k^j v_m^j \vec{d}_k \cdot \vec{d}_m. \quad (16)$$

Thus, we obtain the integrationally averaged squares of dipole moments in the eigenbasis $\bar{\mu}^2/d^2 = \{0.25, 0.64, 0.39, 0.11, 0.62, 0.12, 0.20\}$, where the eigenenergies increase from left to right. For an appropriate d , these values are in rough agreement with the averaged dipole moments obtained from a fit to the experimental spectrum $\mu_{\text{FIT}}^2 = \{49, 87, 73, 31, 82, 24, 36\}$ debye² [14].

However, we can also read the result as $\bar{\mu}_{E_j}^2 = \frac{1}{3} \sum_{k,m=1}^7 v_k^j v_m^j \sum_{i=1}^3 \vec{d}_k \cdot \vec{l}_i \vec{d}_m \cdot \vec{l}_i$, where the three polarization vectors \vec{l}_i are orthogonal to each other. This now implies that the rotational average can be performed using three orthogonal directions for \vec{l} instead of sampling over the whole unit sphere. Note that this calculation is valid only if the interaction of the system and the bath does not interfere with the rotational average.

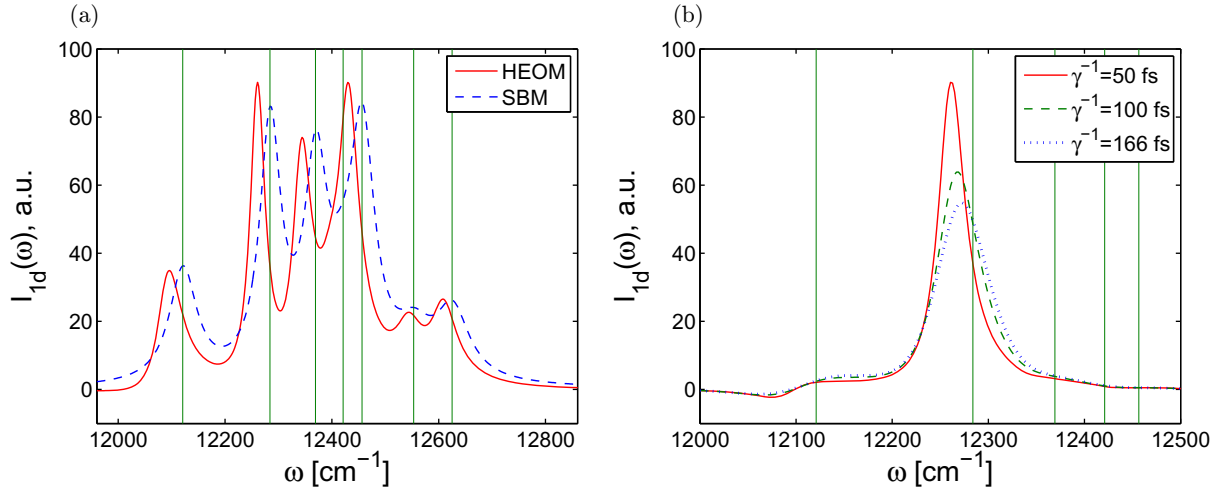


Figure 1. (a) Absorption spectra $I_{ID}(\omega)$ (12) for the FMO complex calculated at $T = 77$ K using the HEOM for $\gamma^{-1} = 50$ fs, $\lambda = 35$ cm^{-1} and μ_{FIT} and the secular Born–Markov (SBM) approximation (without Lamb shift) for $J(\omega) = \lambda\omega/\omega_c e^{-\omega/\omega_c}$, $\omega_c = 150$ cm^{-1} . The vertical lines correspond to the eigenvalues of the exciton Hamiltonian (3). (b) Absorption lines of the second eigenstate calculated using the HEOM for different values of γ^{-1} in the spectral density (2) with fixed $\lambda = 35$ cm^{-1} .

In the following, we discuss how the line shapes of the peaks depend on the theoretical method and approximations commonly used to perform the time-dependent propagation in (12) before we return to different methods of performing the rotational average.

3.1. Absorption spectra obtained by different propagation methods

We calculate the absorption spectra of the FMO complex at the temperature $T = 77$ K. We propagate the exciton–bath system during 2048 fs with a numerical time step of 2 fs using the HEOM with reorganization energy $\lambda = 35$ cm^{-1} and a time scale for the bath correlations given by $\gamma^{-1} = 50$ fs. Each HEOM propagation takes only 1 s on a GPU.

In figure 1(a), we compare the results obtained for the absorption spectrum calculated using the HEOM and the secular Born–Markov (SBM) approximation following [12, 45]. The line shapes for each eigenenergy can be calculated in the eigenbasis $I_j = \int_0^\infty e^{i\omega t} \langle \text{tr}(\mu_{E_j}(t)\mu_{E_j}(0)\rho_0) \rangle_{\text{rot}}$. In the SBM simulation the complete spectrum is identical to the sum of the seven positive absorption peaks (not shown). Owing to the rotating wave approximation the terms $\text{tr}(\mu_{E_j}(t)\mu_{E_l}(0)\rho_0)$ for $j \neq l$ are zero. For the HEOM, these terms have non-vanishing contributions and the sum of the line shapes I_j no longer yields the spectrum. Thus, we have to calculate the line shape of the j th exciton peak as $I_j = \int_0^\infty e^{i\omega t} \langle \text{tr}(\sum_{i=1}^{N_{\text{sites}}} \mu_{E_i}(t)\mu_{E_j}(0)\rho_0) \rangle_{\text{rot}}$. Including these terms leads to more complicated line shapes with shoulders and negative contributions, as shown in figure 1(b) for the peak of the second eigenstate. We find that the more complicated line shapes arise from the non-secular approximations. Comparisons of different shapes of the spectrum obtained by different propagation methods and different spectral densities have been presented in [46, 47] for the B850 ring of the light-harvesting complex LH2.

We observe in figure 1(a) that the energies for the HEOM peaks are shifted compared to the peaks obtained in the SBM approximation. Since we do not take into account the time-dependent Lamb shift in the SBM approximation (see equation (8) of [45]), the corresponding SBM peaks are located at the exciton energies of Hamiltonian (3), marked by the vertical lines. Note that the eigenenergies of Hamiltonian (3) include the reorganization energy λ added to the ‘bare exciton energies’. Due to the dissipation of the reorganization energy within the vibrational environment, taken into account by the HEOM [24], the peaks of the absorption spectrum shift to lower energies. For a fast phonon relaxation $\gamma^{-1} \rightarrow 0$ (Markov limit) the reorganization energy dissipates instantaneously and the peaks are shifted to lower energies by approximately λ and then coincide with the bare exciton energies. Figure 1(b) displays how the bath-correlation time affects the peak shapes and positions. For longer phonon relaxation times, the reorganization energy dissipates slowly during the exciton dynamics and the peaks stay closer to the eigenenergies of (3).

While the spectra shown above are calculated using fitted dipole moments from [14], we will now analyse the changes due to rotational averaging on the absorption spectrum. In figure 2(a) we show the results for the spectrum using the HEOM for $\lambda = 35 \text{ cm}^{-1}$ and $\gamma^{-1} = 166 \text{ fs}$. We compare different methods of rotational average discussed in the previous section, i.e. a single propagation from integrationally averaged dipole moments using $\bar{\mu}$ equation (16), a Monte Carlo (MC) set of 300 orientations and μ_{FIT} . The results using three propagations with perpendicular laser directions xyz are not shown since the curve is almost identical to the MC spectrum for 300 realizations. The MC method matches the experimental conditions closest, since the experiment shows the averaged spectrum of many randomly orientated complexes. To avoid propagating density matrices for many random orientations, the xyz approach can be chosen instead, as both spectra show excellent agreement. Neither the integrated dipole moments nor the fitted ones yield comparable results to the MC method, and only in the Markovian limit it is possible to run the propagation with pre-averaged dipole moments. Here, we chose a longer bath correlation time $\gamma^{-1} = 166 \text{ fs}$ for the comparison of different rotational averages as the differences vanish for decreasing γ^{-1} .

In the following, we always use several orientations for rotational averages and do not resort to pre-averaged dipole moments.

3.2. Broadening of the spectral lines

If we compare the only rotationally averaged absorption spectra in figure 1(a) with the experimentally measured ones [14], we find that the rotationally averaged peaks are too narrow. Furthermore, six peaks are well pronounced while in experiments several peaks overlap and the third exciton eigenstate is not individually resolved. This result is expected, since there are several additional effects in addition to rotational averaging, which broaden the peaks and bring the simulation results closer to the experimental data. If we increase either λ (not shown) or the relaxation time γ^{-1} , the peaks in the spectrum become broader, see figure 1(b). Both parameters change the spectral density and hence the coupling to the vibrational modes. The third mechanism is static disorder caused by the slowly fluctuating protein environment. We model the static disorder by adding a Gaussian distributed noise of a given standard deviation (SD) to each diagonal term in (3). The resulting spectra are shown in figure 2(b) where we obtain broader peaks and show with increasing disorder the diminishing of the third peak in the spectrum. In addition, we observe that the broadening changes the relative peak heights of the second and the fourth peaks yielding better agreement with the experimental results.

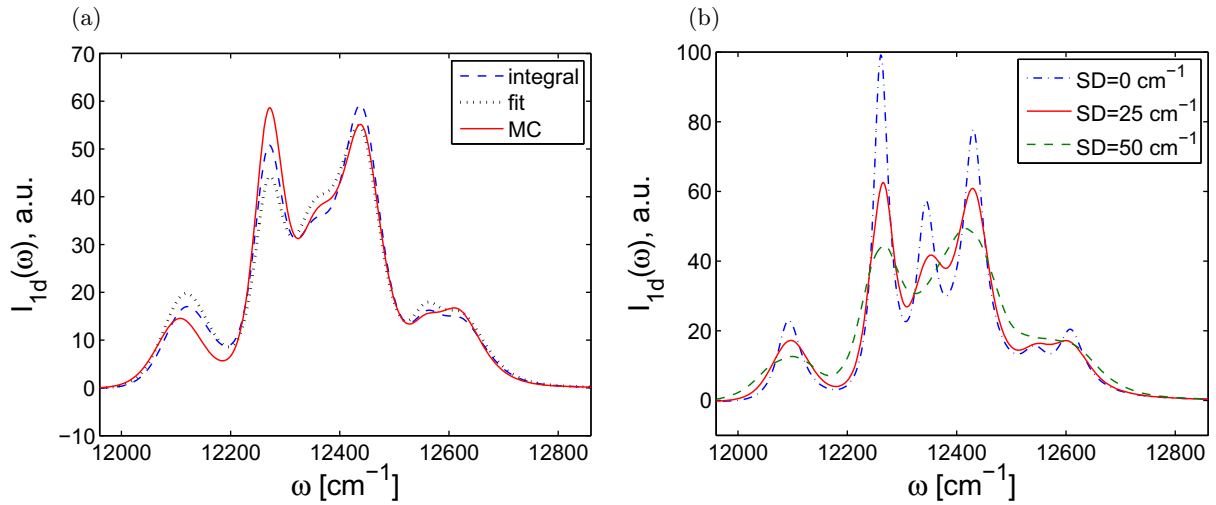


Figure 2. (a) Absorption spectra $I_{1D}(\omega)$ of the FMO complex calculated using the HEOM with $N_{\max} = 8$ at $T = 77$ K, $\lambda = 35$ cm^{-1} and $\gamma^{-1} = 166$ fs. We compare different methods of performing the rotational average in the calculations. The dotted line results from using the fitted values μ_{FIT} and the dashed line takes the values $\bar{\mu}$. The solid line denotes an MC average over 300 samples. The spectra are normalized with respect to the area under the graph. (b) Comparison of the absorption spectra for $\gamma^{-1} = 50$ fs for different values of static Gaussian disorder, which is characterized by its SD. In all cases the rotational average was performed with MC using 300 realizations.

For the absorption spectrum, changing the spectral density and inhomogeneous broadening yields similar results and it is not possible to distinguish which mechanism is relevant for the FMO complex. It is in the 2D echo-spectra where the difference becomes visible since the disorder results in a broadening along the diagonal frequencies only, while changing the exciton–phonon coupling broadens the peaks in all directions [48].

4. Two-dimensional (2D) echo-spectroscopy

In addition to the information provided by absorption spectroscopy, 2D echo-spectroscopy is used to study time-resolved processes such as energy transfer or vibrational decay as well as to measure intermolecular coupling strengths [49–51]. 2D echo-spectroscopy consists of a sequence of three ultra-short pulses and a resulting signal pulse with fixed time delay between the second pulse and the third [52, 53]. The theory of 2D echo-spectroscopy is explained in detail in [54–56]. The 2D echo-spectra are measured in two configurations that correspond to the rephasing (RP) and non-rephasing (NR) contributions of the third-order response function

$$S^{(3)}(t_3, t_2, t_1) = \left(\frac{i}{\hbar}\right)^3 \Theta(t_3)\Theta(t_2)\Theta(t_1) \text{tr}(\mu(t_3 + t_2 + t_1) [\mu(t_2 + t_1), [\mu(t_1), [\mu(0), \rho_0]]]) . \quad (17)$$

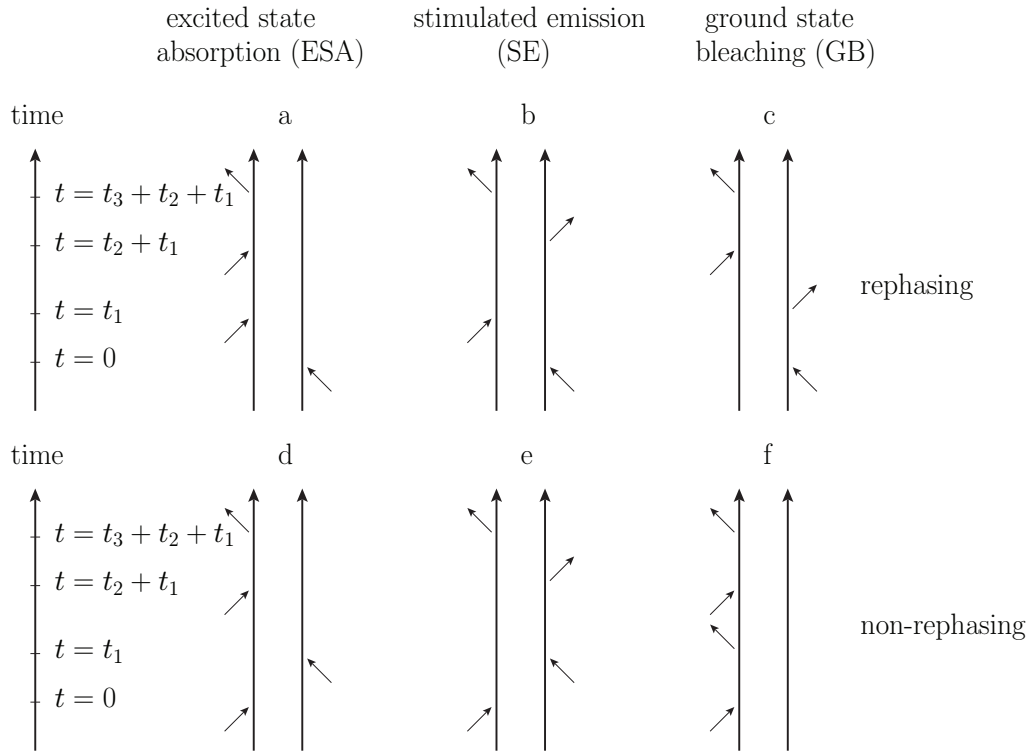


Figure 3. The six Feynman diagrams included in the 2D echo-spectrum calculation. The vertical axis represents the time propagation and the action of the dipole operators is shown by diagonal arrows. For a complete theoretical description, see [55].

Using the impulsive approximation which assumes δ -functions for the temporal envelopes of the pulses, the two components of the spectrum corresponding to $S^{(3)}(t_3, t_2, t_1) = S_{\text{RP}}^{(3)}(t_3, t_2, t_1) + S_{\text{NR}}^{(3)}(t_3, t_2, t_1)$ read

$$I_{\text{RP}}(\omega_3, t_2, \omega_1) = \int_{-\infty}^{\infty} dt_1 \int_{-\infty}^{\infty} dt_3 e^{i\omega_3 t_3 - i\omega_1 t_1} S_{\text{RP}}^{(3)}(t_3, t_2, t_1), \quad (18)$$

$$I_{\text{NR}}(\omega_3, t_2, \omega_1) = \int_{-\infty}^{\infty} dt_1 \int_{-\infty}^{\infty} dt_3 e^{i\omega_3 t_3 + i\omega_1 t_1} S_{\text{NR}}^{(3)}(t_3, t_2, t_1). \quad (19)$$

Sorting this expression for the rephasing and the non-rephasing parts yields six different pathways, which represent the stimulated emission, the ground-state bleach and the excited state absorption [54–57], shown schematically in figure 3. By taking the time between the second and the third pulses as a control parameter as was done in (18) and (19), one can study the exciton dynamics which is probed by recording the emitted signal pulse. Owing to the excited state absorption the dynamics is more involved compared to the one-dimensional case. Including a double-excited manifold, we construct an enlarged exciton Hamiltonian $H_e^{2\text{D}}$ which is block diagonal and of the form

$$H_e^{2\text{D}} = \begin{pmatrix} H_e^{\text{gs}} & 0 & 0 \\ 0 & H_e^{1\text{ex}} & 0 \\ 0 & 0 & H_e^{2\text{ex}} \end{pmatrix}, \quad (20)$$

where $H_e^{\text{gs}} = 0$ represents the ground state, H_e^{1ex} is the single-exciton Hamiltonian with N_{sites}^2 elements as defined in (3), and the energy levels of the two excitons are described by H_e^{2ex} . The two-exciton Hamiltonian H_e^{2D} has $[N_{\text{sites}}(N_{\text{sites}} - 1)/2]^2$ entries which are constructed from the matrix elements of H_e^{1ex} following [14, 54]. For the FMO complex H_e^{2D} is a 29×29 matrix. In site basis, we denote the two exciton states by $|ij\rangle$, where $0 < i < j \leq N_{\text{sites}}$, and the diagonal entries of H_e^{2ex} are given by

$$\langle ij | H_e^{\text{2ex}} | ij \rangle = \langle i | H_e^{\text{1ex}} | i \rangle + \langle j | H_e^{\text{1ex}} | j \rangle. \quad (21)$$

The off-diagonal elements are given by

$$\begin{aligned} \langle ij | H_e^{\text{2ex}} | kl \rangle = & \delta_{ik}(1 - \delta_{jl}) \langle j | H_e^{\text{1ex}} | l \rangle + \delta_{il}(1 - \delta_{jk}) \langle j | H_e^{\text{1ex}} | k \rangle \\ & + \delta_{jk}(1 - \delta_{il}) \langle i | H_e^{\text{1ex}} | l \rangle + \delta_{jl}(1 - \delta_{ik}) \langle i | H_e^{\text{1ex}} | k \rangle. \end{aligned} \quad (22)$$

Physically, this means that the $|ij\rangle$ and $|kl\rangle$ two-exciton states are coupled if they have one exciton in common, while a second exciton is shifted from one site to another. The coupling constant is the same as that for the transition of the corresponding exciton shift in the one-exciton dynamics. Note also that the linear coupling to the independent baths, each of them associated with one BChl, leads to couplings between the one-exciton state $|i\rangle$ and the two-exciton states $|ij\rangle$, which both influence the bath at site i and are in turn influenced by the bath correlations.

Following [31], we construct the dipole operator associated with the extended Hamiltonian (20)

$$\mu = \begin{pmatrix} 0 & \mu_{\text{1ex}}^- & 0 \\ \mu_{\text{1ex}}^+ & 0 & \mu_{\text{2ex}}^- \\ 0 & \mu_{\text{2ex}}^+ & 0 \end{pmatrix}. \quad (23)$$

The zero to single excitation operators μ_{1ex}^\pm are defined as in (10) and (11). The single to double excitation operators are defined according to $\langle ij | \mu_{\text{2ex}}^+ | k \rangle = \delta_{ik} \langle j | \mu_{\text{1ex}}^+ | 0 \rangle + \delta_{jk} \langle i | \mu_{\text{1ex}}^+ | 0 \rangle$ and $\mu_{\text{2ex}}^- = (\mu_{\text{2ex}}^+)^\top$.

In order to calculate 2D spectra, we have to evolve the 29×29 density matrix to obtain the third-order response function $S^{(3)}$. The hierarchical method incorporates the effect of the baths through the auxiliary system of the σ -matrices. When calculating the 2D spectra, we propagate according to the Feynman diagrams shown in figure 3 and let the dipole operator act on the density matrix and the auxiliary matrices to simulate the interaction with the laser field.

We observe in (17) that the 2D spectra depend on the fourth-order dipole moments. To take into account the random orientation of the samples we need to compute rotational averages $\langle \mu_i^2 \mu_j^2 \rangle_{\text{rot}}$, which are performed by sampling ten laser polarization vectors aligned with the vertices of a dodecahedron in one-half of the coordinate space. We take the vertices $(\pm 1, \pm 1, 1)$, $(0, \pm \frac{1}{\phi}, \phi)$, $(\pm \frac{1}{\phi}, \phi, 0)$ and $(\pm \phi, 0, \frac{1}{\phi})$, where $\phi = \frac{1}{2}(1 + \sqrt{5})$ denotes the golden ratio. We have compared the dodecahedral summation with the full spherical averaging using a 10 000-shoot MC and obtain differences of less than 1% of the MC results.

4.1. Numerical results for the 2D echo-spectrum of the FMO complex

For the simulation of 2D spectra, we calculate the third-order response function $S^{(3)}(t_1, t_2, t_3)$ in (17). We obtain 128^2 data points with a spacing of 16 fs in the t_1 and t_3 directions using a numerical time step of 2 fs. This means that we have to perform over 131 000 propagation steps

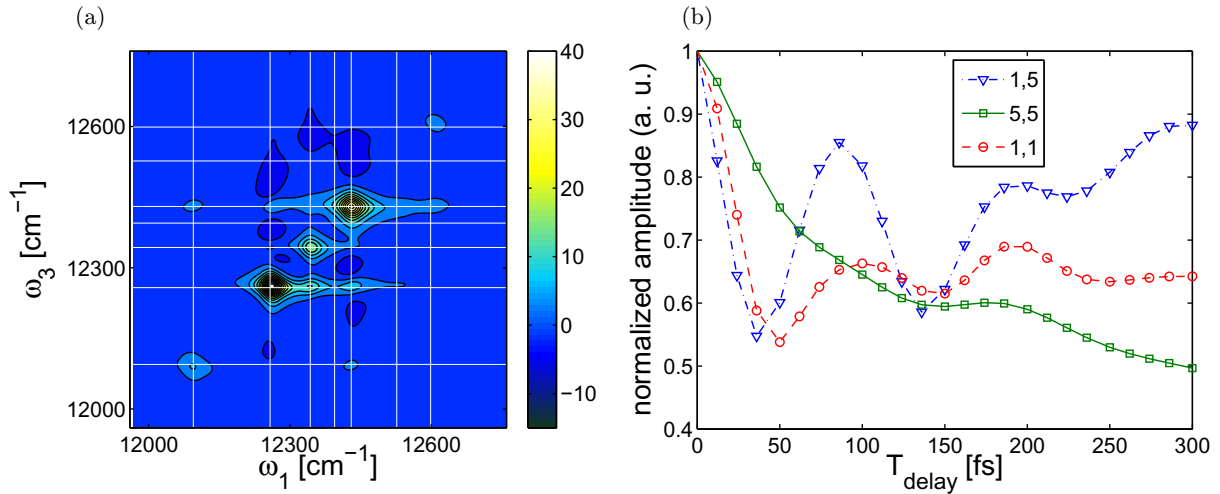


Figure 4. (a) Rotationally averaged 2D spectrum $\text{Re}[I_{\text{NR}} + I_{\text{RP}}]$ of the FMO complex calculated using the HEOM with $\lambda = 35 \text{ cm}^{-1}$, $T = 77 \text{ K}$ and $\gamma^{-1} = 50 \text{ fs}$ and a delay time $T_{\text{delay}} = 0 \text{ fs}$. (b) Oscillations as a function of the delay time for the (1, 1) and (5, 5) diagonal peak and the (1, 5) peak below the diagonal. The points have been connected to guide the eye.

for each of the six Feynman diagrams. Depending on the delay time $T_{\text{delay}} = t_2$ our simulations take 48–53 min on a single NVIDIA Fermi C2050 GPU, which provides a 38-fold speedup compared to the CPU algorithm with filtering methods that reduce the hierarchy [17]. We always show the sum of the real parts of the rephasing and the non-rephasing spectra.

Figure 4(a) shows a simulated 2D spectrum for a rotationally averaged sample with no disorder at $T = 77 \text{ K}$. The figure is encoded using a linear colour scale. We divided the raw data by a constant to obtain an amplitude on a -10 to 40 range. The thin white lines have been added to indicate the expected peak positions. The peaks are denoted by their excitonic energy-level indices (i, j) , with the first number referring to the ω_3 -axis and the second one to the ω_1 -axis. The spectrum shows similarities to the experimentally measured one in [14] insofar as it reproduces the large peak on the diagonal at the second eigenstate and a second near the fourth and the fifth. Furthermore, we find negative amplitudes above the diagonal and positive peaks below. As expected from the discussion of the absorption spectrum in section 3.2, the peak shapes differ from the experimental ones due to the lack of static disorder.

Figure 4(b) shows the peak oscillations for the diagonal peaks (1, 1) and (5, 5) and the off-diagonal peak (1, 5) below the diagonal. We renormalized the peak heights at $T_{\text{delay}} = 0 \text{ fs}$ to unity such that the time-resolved amplitude of the three peaks are conveniently put into the same panel. We choose these peaks because figure 4(a) shows peak (1, 5) as the highest off-diagonal peak in the line where ω_3 is equal to the lowest-lying eigenstate. We see that diagonal and off-diagonal peaks oscillate in time. This indicates that our model imitates the coherent energy transport within the FMO complex that has been observed experimentally [5, 6]. Theoretically, an off-diagonal peak (i, j) is expected to undergo oscillations with a frequency corresponding to the difference of its excitonic eigenenergies $(E_j - E_i)$. For the (1, 5) peak we expect a period of 99 fs, which is in good agreement with our numerical result yielding a best-fit period of 97 fs. When we calculate the peak heights, we integrate over squares of width $\Delta\omega = 16 \text{ cm}^{-1}$

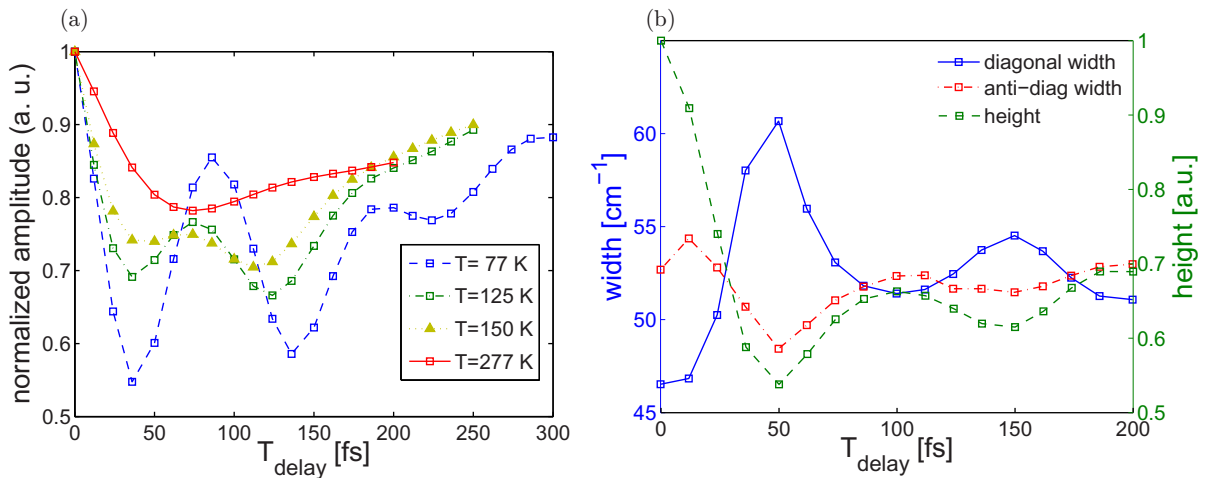


Figure 5. (a) Amplitude of the cross peak (1, 5) of the rotationally averaged spectra of the FMO complex as a function of delay time for different temperatures. (b) Oscillations in the peak width of the (1, 1) diagonal peak measured in the diagonal and anti-diagonal directions compared to the peak height at $T = 77$ K. The points have been connected to guide the eye.

centred around the white crosses. We follow the changes of the peak heights with increasing delay time by plotting the absolute value of the spectrum normalized with respect to the value at $T_{\text{delay}} = 0$ fs.

In order to analyse the robustness of the peak oscillations when the thermal fluctuations increase, we plot in figure 5(a) the oscillations of the (1, 5) cross peak for several temperatures. We compare with the experimental data in [6] and observe qualitatively similar behaviour with weaker oscillations and faster decay when the temperature is increased. We do not obtain the picosecond-lasting beatings that have been observed experimentally. One possible factor is the shape of the spectral density that is used for the HEOM. We fit the oscillations in figure 5(a) by an exponentially decaying sine. The fit is done separately for the stimulated emission and excited state absorption pathway, which couple to one or two baths, respectively. Based on the damping of the oscillations on peak (1, 5) the temperature dependence of the dephasing rate of our simulation is given by $\gamma_{\text{deph}}^{\text{ESA}}(T)/T = (0.66 \pm 0.05) \text{ cm}^{-1} \text{ K}^{-1}$ and $\gamma_{\text{deph}}^{\text{SE}}(T)/T = (0.50 \pm 0.03) \text{ cm}^{-1} \text{ K}^{-1}$. This is in good agreement with what we expect for the chosen spectral density ($2k_{\text{B}}\lambda/(\gamma T) = 0.46 \text{ cm}^{-1} \text{ K}^{-1}$) and the value $0.52 \text{ cm}^{-1} \text{ K}^{-1}$ determined from the experimentally measured data [6].

In the experiments an anti-correlation in peak shapes between the diagonal peak width and the height [5] or alternatively the ratio of the diagonal peak width to the anti-diagonal width and height [4] has been found. The width was measured by fitting a Gaussian to a diagonal cut through the spectrum and taking its SD. Applying the same procedure to the simulation data yields also anti-correlations shown in figure 5(b).

Next, we analyse the role of static disorder in the results for the 2D echo-spectra. When including static disorder, the peaks get elongated along the diagonal as observed when comparing the spectra at zero delay time shown in figures 4(a) and 6(a) and (b) for increasing values of disorder. The plots with disorder show better agreement with the experiment [14].

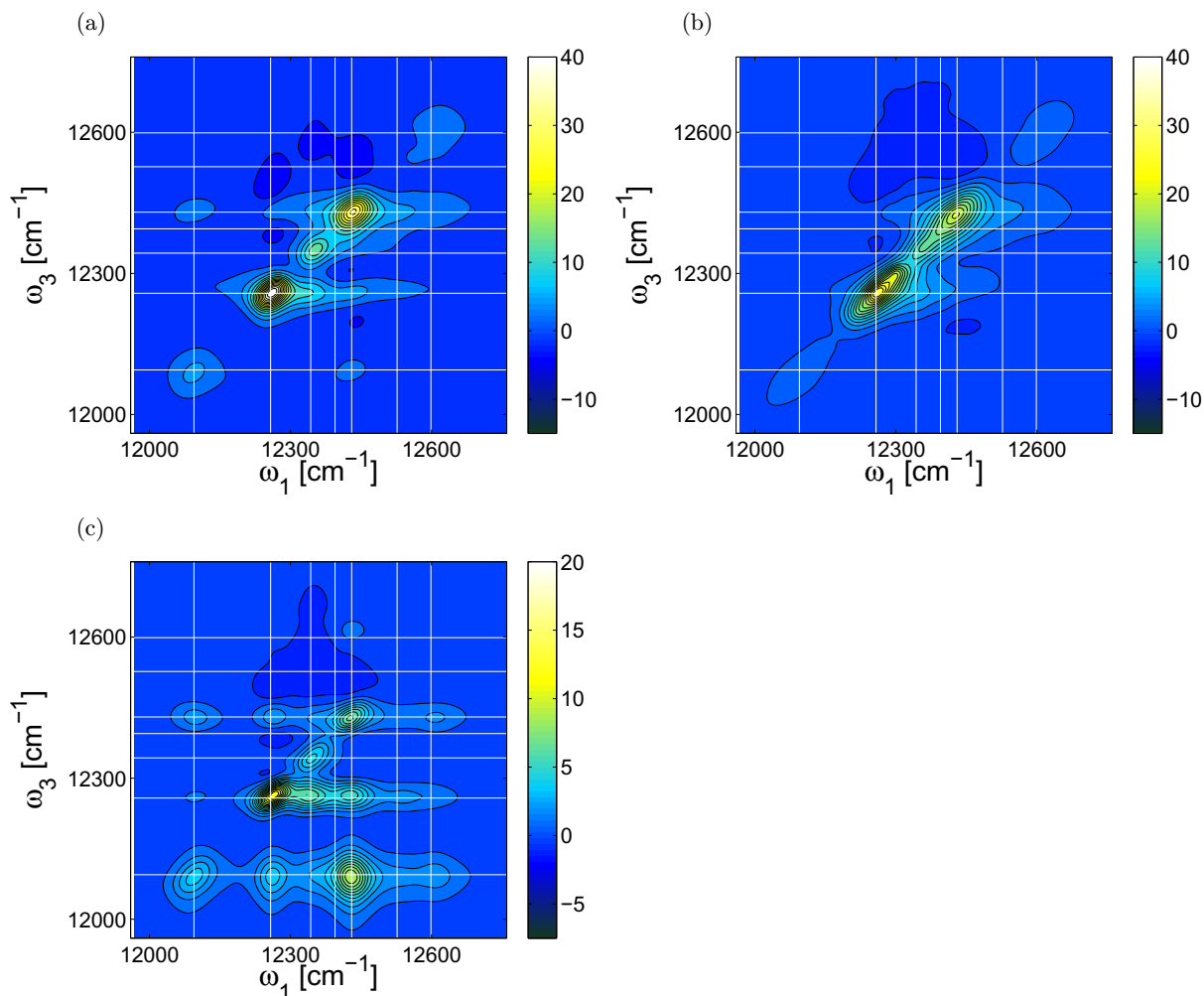


Figure 6. 2D echo-spectra $\text{Re}[I_{\text{NR}} + I_{\text{RP}}]$ of the FMO complex with rotational and disorder averages at temperature $T = 77$ K. The averages are performed over 400 realizations. The spectral-density parameters are $\lambda = 35$ cm $^{-1}$ and $\gamma^{-1} = 50$ fs. (a) Gaussian disorder with SD 25 cm $^{-1}$ at delay time $T_{\text{delay}} = 0$ fs. (b) SD= 50 cm $^{-1}$, $T_{\text{delay}} = 0$ fs. (c) SD= 25 cm $^{-1}$, $T_{\text{delay}} = 4000$ fs.

Figure 6(c) shows the 2D spectra for $\text{SD} = 25$ cm $^{-1}$ for a long delay time $T_{\text{delay}} = 4000$ fs for which the system approaches its thermal stationary state. We observe that the excitation moves from the diagonal peaks into the regions with lower frequency ω_3 . This occurs as the system relaxes to lower-lying eigenstates during the delay time. In experiments by Brixner *et al* [9] the decay of the population into the ground state of the system is also visible.

The absence of the experimentally seen oscillation in the HEOM calculation in [17] has led Chen *et al* to conclude that the importance of static disorder requires careful reconsideration. First-principles simulations of static disorder in the FMO complex are computationally extremely time-consuming, since several hundreds of realizations are required to reach converged results. In order to study the role of static disorder in the oscillations of the peaks of the spectrum and to ensure numerical convergence, we construct a dimer to model the (1, 5)

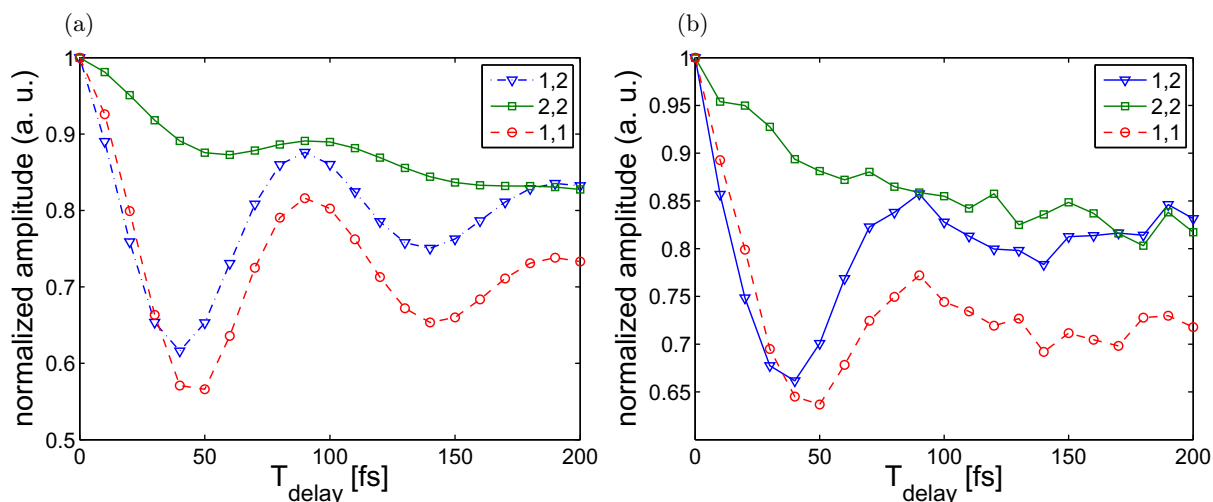


Figure 7. Peak oscillations in a model dimer for $T = 77$ K, $\lambda = 35$ cm $^{-1}$ and $\gamma^{-1} = 50$ fs. To concentrate on the disorder effects, no rotational average is performed and the calculation is performed using $\mu_1 = -5.4$ and $\mu_2 = 12.2$: (a) no static disorder and (b) Gaussian disorder with SD 25 cm $^{-1}$. The average was done over 1000 realizations at each delay time. The points have been connected to guide the eye.

peak of the FMO spectrum. For the model dimer we chose the Hamiltonian such that the first and fifth FMO complex eigenvalues are reproduced. The coupling between both sites is set to 50 cm $^{-1}$. The simulations with and without disorder show oscillations on the diagonal and off-diagonal peaks. The most striking effect of disorder is a decreased oscillatory amplitude. While the cross peak in the simulation without disorder has lost 45% of its amplitude in the first minimum, in the disorder case the loss is only 35%. From a fit, we observe that the periods of the disorder curves are slightly shorter, $T = 92$ and 98 fs for the (1, 1) and (2, 1) curves, while in the no-disorder plot, $T = 95$ and 98 fs has been obtained, respectively (figure 7). For the FMO complex we expect that oscillations are reduced in amplitude by a similar magnitude and therefore still persist within the model.

5. Conclusions

We have presented calculations of the absorption spectra and 2D echo-spectra for the FMO complex at different temperatures using the HEOM for solving the exciton and the vibrational bath dynamics and adding static disorder to account for the fluctuating environment. Important ingredients necessary to find good agreement with experiments for the absorption spectra using the HEOM propagation method are to perform the rotational average and to include static disorder. We have also discussed how other simplified propagation methods affect the line shapes and shift the peaks in the spectra.

Our rotationally averaged 2D echo-spectra reflect the main features of the experimentally measured ones. At delay time $T_{\text{delay}} = 0$, we find negative contributions above the diagonal and elongated peaks in the diagonal which are transferred to the lowest exciton states after long times on the picosecond scale. The HEOM method yields oscillatory behaviour of peak amplitudes over a wide temperature range. At $T = 77$ K we obtain oscillations of cross peak

amplitudes up to 300 fs with the expected frequency that corresponds to the difference in excitonic eigenenergies. In addition, oscillations on the diagonal peaks are present. The long duration of oscillations in the experimental data (up to 1.8 ps in [6]) suggests that further refinements of the theoretical models are necessary, for example by adjusting the form of the spectral density that affects the population dynamics [38].

Remarkably, we find excellent agreement with the measured damping rate of the oscillations due to thermal fluctuations. This implies a good choice of the parameters of the model and might explain why we obtain different results compared to previous calculations, which were performed at a higher value of $\gamma^{-1} = 100$ fs [17], leading to an increased dephasing by a factor of two. At ambient temperatures the HEOM have the advantage of requiring fewer terms to converge, while approximate methods such as the secular and full Redfield approximations do not yield the correct time evolution of the density matrix and overestimate the thermalization rate.

In agreement with the experimental measurements, we observe the anti-correlated oscillations of the peak heights and peak shapes for the diagonal peaks. The analysis of a model dimer shows that the cross peak oscillations persist even in the presence of static disorder, which mainly results in a reduction of oscillation amplitude by about 30%.

Acknowledgments

This work was supported by the Emmy-Noether programme of the DFG (KR 2889/2), the DAAD project 50240755, the Spanish MINCINN AI DE2009-0088 (Acciones Integradas Hispano-Alemanas), the Spanish MICINN project FIS2010-18799 and the Ramón y Cajal programme. We thank Akihito Ishizaki for helpful discussions. Time on the Harvard School of Engineering and Applied Sciences ‘Resonance’ GPU cluster and support by the SEAS Academic Computing team are gratefully acknowledged.

References

- [1] Ishizaki A, Calhoun T R, Schlau-Cohen G S and Fleming G R 2010 Quantum coherence and its interplay with protein environments in photosynthetic electronic energy transfer *Phys. Chem. Chem. Phys.* **12** 7319
- [2] Fenna R E and Matthews B W 1975 Chlorophyll arrangement in a bacteriochlorophyll protein from *Chlorobium limicola* *Nature* **258** 573
- [3] Sybesma C and Olson J M 1963 Transfer of chlorophyll excitation energy in green photosynthetic bacteria *Proc. Natl Acad. Sci. USA* **49** 248–53
- [4] Collini E, Wong C Y, Wilk K E, Curmi P M G, Brumer P and Scholes G D 2010 Coherently wired light-harvesting in photosynthetic marine algae at ambient temperature *Nature* **463** 644
- [5] Engel G S, Calhoun T R, Read E L, Ahn T-K, Mančal T, Cheng Y-C, Blankenship R E and Fleming G R 2007 Evidence for wavelike energy transfer through quantum coherence in photosynthetic systems *Nature* **446** 782
- [6] Panitchayangkoon G, Hayes D, Fransted K A, Caram J R, Harel E, Wen J, Blankenship R E and Engel G S 2010 Long-lived quantum coherence in photosynthetic complexes at physiological temperature *Proc. Natl Acad. Sci. USA* **107** 12766
- [7] Olbrich C, Jansen T, Liebers J, Aghtar M, Strumpfer J, Schulten K, Knoester J and Kleinekathoefer U 2011 From atomistic modeling to excitation transfer and two-dimensional spectra of the FMO light-harvesting complex *J. Phys. Chem. B* **115** 8609–21

- [8] Shim S, Rebentrost P, Valleau S and Aspuru-Guzik A 2011 Microscopic origin of the long-lived quantum coherences in the Fenna–Matthew–Olson complex arXiv:1104.2943v1
- [9] Brixner T, Stenger J, Vaswani H M, Cho M, Blankenship R E and Fleming G R 2005 Two-dimensional spectroscopy of electronic couplings in photosynthesis *Nature* **434** 625
- [10] Mohseni M, Rebentrost P, Lloyd S and Aspuru-Guzik A 2008 Environment-assisted quantum walks in photosynthetic energy transfer *J. Chem. Phys.* **129** 174106
- [11] Caruso F, Chin A, Datta A, Huelga S F and Plenio M B 2009 Highly efficient energy excitation transfer in light-harvesting complexes: the fundamental role of noise-assisted transport *J. Chem. Phys.* **131** 105106
- [12] Kreisbeck C, Kramer T, Rodríguez M and Hein B 2011 High-performance solution of hierarchical equations of motions for studying energy-transfer in light-harvesting complexes *J. Chem. Theory Comput.* **7** 2166
- [13] Yuen-Zhou J and Aspuru-Guzik A 2011 Quantum process tomography of excitonic dimers from two-dimensional electronic spectroscopy. I. General theory and application to homodimers *J. Chem. Phys.* **134** 134505
- [14] Cho M, Vaswani H M, Brixner T, Stenger J and Fleming G R 2005 Exciton analysis in 2D electronic spectroscopy *J. Phys. Chem. B* **109** 10542
- [15] Brüggemann B, Kjellberg P and Pullerits T 2007 Non-perturbative calculation of 2D spectra in heterogeneous systems Exciton relaxation in the FMO complex *Chem. Phys. Lett.* **444** 192–6
- [16] Sharp L Z, Egorova D and Domcke W 2010 Efficient and accurate simulations of two-dimensional electronic photon-echo signals: illustration for a simple model of the Fenna–Matthews–Olson complex *J. Chem. Phys.* **132** 014501
- [17] Chen L, Zheng R, Jing Y and Shi Q 2011 Simulation of the two-dimensional electronic spectra of the Fenna–Matthews–Olson complex using the hierarchical equations of motion method *J. Chem. Phys.* **134** 194508
- [18] Thorwart M, Eckel J, Reina J H, Nalbach P and Weiss S 2009 Enhanced quantum entanglement in the non-Markovian dynamics of biomolecular excitons *Chem. Phys. Lett.* **478** 234–7
- [19] Tanimura Y and Kubo R 1989 Time evolution of a quantum system in contact with a nearly Gaussian–Markoffian noise bath *J. Phys. Soc. Japan* **58** 101–14
- [20] Yan Y, Yang F, Liu Y and Shao J 2004 Hierarchical approach based on stochastic decoupling to dissipative systems *Chem. Phys. Lett.* **395** 216
- [21] Xu R-X, Cui P, Li X-Q, Mo Y and Yan Y J 2005 Exact quantum master equation via the calculus on path integrals *J. Chem. Phys.* **122** 041103
- [22] Ishizaki A and Tanimura Y 2005 Quantum dynamics of system strongly coupled to low-temperature colored noise bath: reduced hierarchy equations approach *J. Phys. Soc. Japan* **74** 3131
- [23] Tanimura Y 2006 Stochastic Liouville, Langevin, Fokker–Planck and master equation approaches to quantum dissipative systems *J. Phys. Soc. Japan* **75** 082001
- [24] Ishizaki A and Fleming G R 2009 Unified treatment of quantum coherent and incoherent hopping dynamics in electronic energy transfer: reduced hierarchy equation approach *J. Chem. Phys.* **130** 234111
- [25] Ishizaki A and Fleming G R 2009 Theoretical examination of quantum coherence in a photosynthetic system at physiological temperature *Proc. Natl Acad. Sci. USA* **106** 17255
- [26] Tronrud D E, Wen J, Gay L and Blankenship R E 2009 The structural basis for the difference in absorbance spectra for the FMO antenna protein from various green sulfur bacteria *Photosynth. Res.* **100** 79–87
- [27] Ben-Shem A, Frolow F and Nelson N 2004 Evolution of photosystem I—from symmetry through pseudosymmetry to asymmetry *FEBS Lett.* **564** 274
- [28] Schmidt am Busch M, Müh FEI-Amine Madjet M and Renger T 2011 The eighth bacteriochlorophyll completes the excitation energy funnel in the FMO protein *J. Phys. Chem. Lett.* **2** 93
- [29] Leegwater J A 1996 Coherent versus incoherent energy transfer and trapping in photosynthetic antenna complexes *J. Phys. Chem.* **100** 14403
- [30] Ritz T, Park S and Schulten K 2001 Kinetics of excitation migration and trapping in the photosynthetic unit of purple bacteria *J. Phys. Chem. B* **105** 8259

- [31] May V and Kühn O 2004 *Charge and Energy Transfer Dynamics in Molecular Systems* (Weinheim: Wiley-VCH)
- [32] Yang M and Fleming G R 2002 Influence of phonons on exciton transfer dynamics: comparison of the Redfield, Förster, and modified Redfield equations *Chem. Phys.* **275** 355
- [33] Adolphs J and Renger T 2006 How proteins trigger excitation energy transfer in the FMO complex of green sulfur bacteria *Biophys. J.* **91** 2778
- [34] Olbrich C, Strümpfer J, Schulten K and Kleinekathöfer U 2011 Theory and simulation of the environmental effects on FMO electronic transitions *J. Phys. Chem. Lett.* **2** 1771–6
- [35] Vulto S I E, de Baat M A, Louwe R J W, Permentier H P, Neef T, Miller M, van Amerongen H and Aartsma T J 1998 Exciton simulations of optical spectra of the FMO complex from the green sulfur bacterium *chlorobium tepidum* at 6 K *J. Phys. Chem. B* **102** 9577–82
- [36] Vulto S I E, de Baat M A, Neerken S, Nowak F R, van Amerongen H, Amesz J and Aartsma T J 1999 Excited state dynamics in FMO antenna complexes from photosynthetic green sulfur bacteria: a kinetic model *J. Phys. Chem. B* **103** 8153–61
- [37] Wendling M, Pullerits T, Przyjalowski M A, Vulto S I E, Aartsma T J, van Grondelle R and van Amerongen H 2000 Electron-vibrational coupling in the Fenna–Matthews–Olson complex of *Prosthecochloris aestuarii* determined by temperature-dependent absorption and fluorescence line-narrowing measurements *J. Phys. Chem. B* **104** 5825
- [38] Nalbach P, Braun D and Thorwart M 2011 Exciton transfer dynamics and quantumness of energy transfer in the Fenna–Matthews–Olson complex *Phys. Rev. E* **84** 041926
- [39] Hu J, Xu R-X and Yan Y J 2010 Communication: Padé spectrum decomposition Fermi function and Bose function *J. Chem. Phys.* **133** 101106
- [40] Hu J, Luo M, Jiang F, Xu R-X and Yan Y J 2011 Padé spectrum decompositions of quantum distribution functions and optimal hierarchical equations of motion construction for quantum open systems *J. Chem. Phys.* **134** 244106
- [41] Shi Q, Chen L, Nan G, Xu R-X and Yan Y J 2009 Efficient hierarchical Liouville space propagator to quantum dissipative dynamics *J. Chem. Phys.* **130** 084105
- [42] Zhu J, Kais S, Rebentrost P and Aspuru-Guzik A 2011 Modified scaled hierarchical equation of motion approach for the study of quantum coherence in photosynthetic complexes *J. Phys. Chem. B* **115** 1531
- [43] Adolphs J, Müh F, El-Amine Madjet M and Renger T 2008 Calculation of pigment transition energies in the FMO protein: from simplicity to complexity and back *Photosynth. Res.* **95** 197–209
- [44] Berman H M, Westbrook J, Feng Z, Gilliland G, Bhat T N, Weissig H, Shindyalov I N and Bourne P E 2000 The Protein Data Bank *Nucl. Acids Res.* **28** 235–42
- [45] Rebentrost P, Chakraborty R and Aspuru-Guzik A 2009 Non-Markovian quantum jumps in excitonic energy transfer *J. Chem. Phys.* **131** 184102
- [46] Schröder M, Kleinekathöfer U and Schreiber M 2006 Calculation of absorption spectra for light-harvesting systems using non-Markovian approaches as well as modified Redfield theory *J. Chem. Phys.* **124** 084903
- [47] Chen L, Zheng R, Shi Q and Yan Y 2009 Optical line shapes of molecular aggregates: hierarchical equations of motion method *J. Chem. Phys.* **131** 094502
- [48] Cho M 2008 Coherent two-dimensional optical spectroscopy *Chem. Rev.* **108** 1331–418
- [49] Tanimura Y and Ishizaki A 2009 Modeling, calculating and analyzing multidimensional vibrational spectroscopies *Acc. Chem. Res.* **42** 1270
- [50] Cho M, Brixner T, Stiopkin I, Vaswani H and Fleming G R 2006 Two dimensional electronic spectroscopy of molecular complexes *J. Chin. Chem. Soc.* **53** 15
- [51] Abramavicius D, Voronine D V and Mukamel S 2008 Double-quantum resonances and exciton-scattering in coherent 2D spectroscopy of photosynthetic complexes *Proc. Natl Acad. Sci. USA* **105** 8525
- [52] Read E L, Lee H and Fleming G R 2009 Photon echo studies of photosynthetic light harvesting *Photosynth. Res.* **101** 233
- [53] Brixner T, Stiopkin I V and Fleming G R 2004 Tunable two-dimensional femtosecond spectroscopy *Opt. Lett.* **29** 884

- [54] Cho M 2009 *Two-Dimensional Optical Spectroscopy* (Boca Raton, FL: CRC Press)
- [55] Mukamel S 1999 *Principles of Nonlinear Optical Spectroscopy* (Oxford: Oxford University Press)
- [56] Hamm P 2005 Principles of nonlinear optical spectroscopy: a practical approach, <http://www.mitr.p.lodz.pl/evu/lectures/Hamm.pdf>
- [57] Chen L, Zheng R, Shi Q and Yan Y J 2010 Two-dimensional electronic spectra from the hierarchical equations of motion method: application to model dimers *J. Chem. Phys.* **132** 024505